J. Mex. Chem. Soc. **2024**, *68*(4)
Special Issue

ISSN-e 2594-0317

Review: Description of Porous Media and their Sorption Characteristics as Correlated Structures

Salomón Cordero-Sánchez[1]*, Juan M. Esparza-Schulz[1], Ilich A. Ibarra[2], Víctor M. Trejos[1], Annabel L. Tellez-Gonzalez[1], Juan Villegas-Cortez[3], Graciela Román-Alonso[4], Salomón J. Alas[5]

[1]Departamento de Química, Universidad Autónoma Metropolitana-Iztapalapa, Ciudad de México 09310, México.
[2]Laboratorio de Fisicoquímica y Reactividad de Superficies (LaFReS), Instituto de Investigaciones en Materiales, Universidad Nacional Autónoma de México, Circuito Exterior s/n, CU, Coyoacán, 04510, Ciudad de México, México. On Sabbatical as "Catedra Dr. Douglas Hugh Everett" at Departamento de Química, Universidad Autónoma Metropolitana-Iztapalapa, Ciudad de México 09310, Mexico.
[3]Departmento de Sistemas, Universidad Autónoma Metropolitana, Av. Sn. Pablo 420, Col Nueva El Rosario, CP 02128, Alc Azcapotzalco, Mexico City, Mexico.
[4]Departamento de Ingeniería Eléctrica, Universidad Autónoma Metropolitana-Iztapalapa, Ciudad de México 09310 México.
[5]Departamento de Ciencias Naturales, Universidad Autónoma Metropolitana Unidad Cuajimalpa, 05300 Ciudad de México, Mexico.

***Corresponding author:** Salomón Cordero-Sánchez; email: scordero@izt.uam.mx

Received May 2nd, 2024; Accepted July 1st, 2024.

DOI: http://dx.doi.org/10.29356/jmcs.v68i4.2269

Abstract. This review presents an in-depth analysis of the progress and achievements in the study of porous structures by the Physicochemical of Surfaces Academic Area at the Universidad Autónoma Metropolitana, Iztapalapa's Chemistry Department. A straightforward model for depicting disordered structures has been introduced here, facilitating the discovery of correlations between adjacent elements within these structures. Such correlations have proven to be crucial in the classification and analysis of different disordered porous materials and have been instrumental in the interpretation and categorization of nitrogen adsorption isotherms.
Keywords: Adsorption isotherms; Physicochemical of surfaces academic area, and porous media.

Resumen. Este artículo proporciona una revisión completa de los avances y aportes realizados en la caracterización de estructuras porosas dentro del Área Académica de Fisicoquímica de Superficies del Departamento de Química de la Universidad Autónoma Metropolitana, Iztapalapa. Dentro de esta Área Académica se ha desarrollado un modelo simple para describir estructuras desordenadas, que permitió visualizar la correlación entre elementos vecinos que constituyen dichas estructuras. Estas correlaciones han resultado en un factor clave para clasificar y categorizar diversos medios porosos desordenados, además de servir como herramientas útiles para interpretar y clasificar las isotermas de adsorción del nitrógeno.
Palabras clave: Isotermas de adsorción, área académica de Fisicoquímica de superficies, y medios porosos.

J. Mex. Chem. Soc. **2024**, *68*(4)
Special Issue

ISSN-e 2594-0317

Introduction

Porous media play a crucial role in various technological applications, serving as catalytic supports, membranes, filters, and separation and sensing devices for gas molecules and solutions [1]. In recent years, there has been remarkable advancement in synthesizing modern porous solids with ordered structures, including Mobil Composition of Matter No. 41 (MCM-41), Santa Barbara Amorphous-15 (SBA-15), and Metal-organic frameworks (MOFs) [2-4]. These advancements allow precise characterization of the size and geometrical structures of such materials. The surface area of porous solids can be evaluated through gas adsorption, using the Brunauer-Emmett-Teller (BET) equation, which is widely employed for predicting and explaining the adsorptive properties of solids [5,6]. Additionally, another crucial parameter in characterizing porous solids is the pore size distribution (PSD). Three groups of techniques have become essential tools for determining PSD with high precision. The first group consists of theoretical techniques derived from the classical theory of liquids, known as classical density functional theory (DFT) [7-9]. The second group includes molecular simulation techniques such as Monte Carlo simulations and molecular dynamics simulations based on force fields [10-12]. The third group comprises advanced techniques, including quantum based methods and ab initio molecular dynamics for studying pore size distribution in complex materials [13-16].

However, several decades ago, before the advent of modern solids, it was very difficult to describe in a precise manner the structure of materials such as Vycor glasses, silicas, carbons and clays. And even more complex, to establish a direct correlation between solid structure and the physicochemical phenomena occurring during their technological applications. In this context, numerous scientific efforts aimed to provide a theoretical framework for understanding the effect of pore geometry and interconnection over the most used technique to characterize porous solids: adsorption of gasses. During the 1950s, 1960s and 1970s the study of adsorptive properties in cylindrical pores yielded valuable insights into interpreting adsorption isotherms. Examples include the Barrett-Joyner-Halenda (BJH) method [17], which was widely used for determining PSD; the Broekhoff de Boer description [18], and the studies conducted by Everett and Haynes [19] that delved into the intricate processes of capillary condensation and evaporation of gases that have been adsorbed.

Another significant approach during those days was the development of porous network models. These models aimed to capture the interconnected nature of pore elements using lattices with different geometries. Within such lattices, two key elements are distinguished: sites and bonds. Sites represent points where two or more bonds converge, while bonds are passages connecting two neighbouring sites. Another important characteristic of lattice geometry is the coordination number or connectivity (C), denoting the number of bonds connecting two neighbouring sites. Typically, the connectivity remains constant within each different lattice. In this way, a 3D-lattice can be envisioned as an integrated network of sites and bonds interconnected throughout a volume. Examples of such lattices include the simple cubic lattice (C=6), the body-centered cubic lattice (C=8), and the face-centered cubic lattice (C=12).

By associating sites and bonds with different geometries and sizes, researchers can simulate, besides adsorption, irreversible transport processes in porous media, such as fluid displacement and diffusion of gases and solutions, which remain active fields of research nowadays [20-22]. However, reversible or steady-state processes, such as gas adsorption, represents a formidable challenge. At each equilibrium state, these processes involve an interplay between the geometry of statically confined fluids and the physical attraction between the porous solid walls and the adsorbed gas. Moreover, a confined fluid is not a homogenous phase, since the density of the adsorbed fluid varies as a function of the distance from the solid wall. Nevertheless, in the 1970s, 1980s, and early 1990s, several authors conducted ingenious studies combining simple thermodynamic equations of homogeneous phases and percolation theory applied to porous networks [18-20]. These studies aimed to elucidate the relationship between pore element interconnection, shape, and gas adsorption development. Additionally, methods were developed to calculate the connectivity of porous networks [26]. These methods validated the importance of porous networks as a useful model for interpreting and predicting the shape of adsorbed gas isotherms. During this period, the Academic Area of Physicochemical of Surfaces

J. Mex. Chem. Soc. **2024**, *68*(4)
Special Issue

ISSN-e 2594-0317

(AAPS) developed porous networks embodied with correlation, which are described in detail below. Henceforth, the acronym AAPS will be used.

Dual Site-Bond Model (DSBM)

During the 1980s, the AAPS proposed the Dual Site-Bond Model (DSBM) to describe porous materials with internal structures formed by porous networks composed of interconnected pores and channels, such as Vycor glasses and silica gels [4]. These amorphous materials can be characterized by lattices composed of interconnected sites and bonds. The starting point of the DSBM begins by addressing the relationship between the sizes of interconnected elements that form a porous network. Defining the size of a pore network material is an ambiguous concept. The DSBM resolves this by defining the size of a pore cavity (site) as the radius R_S of the largest sphere that could be accommodated within the cavity. Similarly, the size of a bond is defined as the radius R_B of the largest cylinder that could fit inside the pore channel connecting two sites, or as the radius of the largest circle that would be accommodated inside the pore window connecting two pore cavities. Since a site is a pore element where C-bonds converge, its size must be sufficient to accommodate these bonds. Conversely, since a bond is a channel or a window connecting two sites, its size must be smaller or equal to either of the sites it connects. This leads to the Construction Principle (CP): "the size of any site must always be bigger or at least equal to the size of any of its C-bonds". See Fig. 1 for a schematic representation.

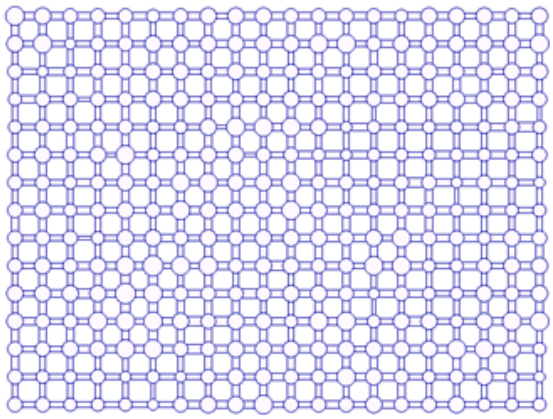

Fig. 1. Schematization of sites and bonds forming a porous network with square geometry. The CP is depicted, showing that the size of any site is always bigger or at least equal to the size of any of its C-bonds.

Two equations ensure the fulfillment of the CP throughout pore networks, given by,

$$B(R) \geq S(R) \tag{1}$$

$$\phi(R_S, R_B) = 0, \forall R_S < R_B \tag{2}$$

where $B(R)$ and $S(R)$ are the fractions of bonds and sites of sizes R_B or R_S smaller or equal to the value R, respectively. Thus, they are defined as the integral of the normalized size probability density functions of sites, $F_S(R_S)$ and bonds, $F_B(R_B)$, as follows,

J. Mex. Chem. Soc. **2024**, *68*(4)
Special Issue

ISSN-e 2594-0317

$$B(R) = \int_0^R F_B(R_B)dR \tag{3}$$

$$S(R) = \int_0^R F_S(R_S)dR \tag{4}$$

Additionally, in Eq. (2) the function $\phi(R_S, R_B)$ is a correlation function that restricts the joint probability, $F(R_S, R_B)$, of finding a site of size $R_S \in (R_S, R_S + dR_S)$ connected to any of its C-bonds of size $R_B \in (R_B, R_B + dR_B)$ in the following way,

$$F(R_S, R_B) = F_S(R_S)F_B(R_B)\phi(R_S, R_B)dR_S dR_B \tag{5}$$

where $\phi(R_S, R_B)$ must satisfy the restriction given by Eq. (2). Then, according to Eq. (5), the joint probability, $F(R_S, R_B)$, becomes equal to zero for $R_B > R_S$. The expression of $\phi(R_S, R_B)$ meeting this latter condition is [27],

$$\phi(R_S, R_B) = \frac{exp\left(-\int_{R_B}^{R_S} \frac{dS}{B(R) - S(R)}\right)}{B(R_S) - S(R_S)} \tag{6}$$

The Eq. (1), often referred to in the literature as the first law of the DSBM, specifies how the functions $F_B(R_B)$ and $F_S(R_S)$ are defined to ensure an adequate quantity of *C*-bonds connected to any site in the pore network. Fig. 2 displays the values of $B(R)$ and $S(R)$ corresponding to three different pairs of the functions F_B and F_S; condition $B(R') \geq S(R'), \forall R'$ is always met for values of R'>0. Additionally, the normalized overlap, Ω, between functions F_B and F_S is presented; note how $\Omega = 0$ in the graphic depicted on the left; $\Omega = 1/3$ (indicated by the red area) for the case in the middle, and $\Omega = 1$ (total overlap between F_B and F_S) in the rightmost case.

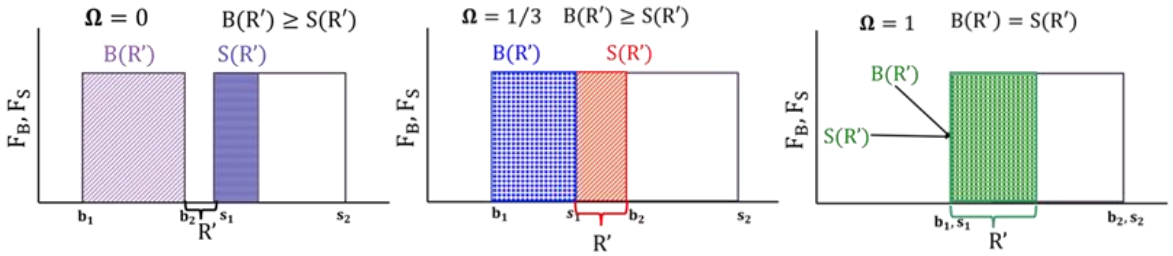

Fig. 2. Illustration of the first law of the DSBM. Each of the uniform distribution functions F_S and F_B satisfy the condition $B(R') \geq S(R'), \forall R'$. The values of B and S corresponds the shaded areas. b_1 (bonds) and s_1 (sites) denote the sizes of the smallest pore elements, whereas b_2 (bonds) and s_2 (sites) correspond to the sizes of the largest pore elements. Parameter Ω represents the normalized area of overlap between F_B and F_S.

On the other hand, Eq. (2), commonly referred to in the literature as the second law of the DSBM, imposes local constraints on connected sites and bonds in order to satisfy the CP. The value of $\phi(R_S, R_B)$ depends on the value of Ω .When $\Omega = 0$, $\phi(R_S, R_B)$ always equals 1, as any bond from $F_B(R_B)$ can be connected to any site with size R_S without violating the CP. However, for $0 < \Omega \leq 1$, the value of of $\phi(R_S, R_B)$ depends

J. Mex. Chem. Soc. **2024**, *68*(4)
Special Issue

ISSN-e 2594-0317

on the specific interval where R_B and R_S are located. Fig. 3 illustrates different values of $\phi(R_S, R_B)$ shown in equation (7), for uniform density distribution functions, resulting from different values of Ω [23-26].

$$\phi(R_S, R_B) = \frac{exp\left(-\int_{R_B}^{R_S} \frac{dS}{B(R) - S(R)}\right)}{B(R_S) - S(R_S)}$$

where

$$\beta(R_S, R_B) = \begin{cases} (R_s - s_1)/(b_2 - s_1) & if \quad R_B \leq s_1 \quad and \quad R_S \leq b_2 \quad (I) \\ 1 & if \quad R_B \leq s_1 \quad and \quad R_S > b_2 \quad (II) \\ (R_s - R_B)/(b_2 - b_1) & if \quad R_B > s_1 \quad and \quad R_S \leq b_2 \quad (III) \\ (b_2 - R_B)/(b_2 - s_1) & if \quad R_B > s_1 \quad and \quad R_S > b_2 \quad (IV) \end{cases}$$

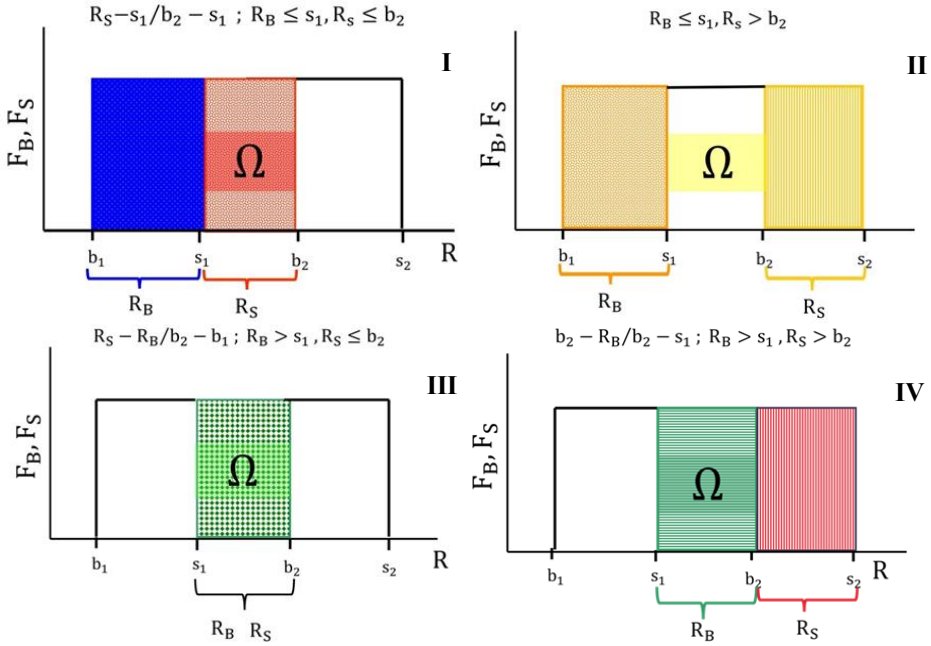

Fig. 3. Different values of $\phi(R_S, R_B)$ for overlapped uniform distribution functions F_B and F_S. Roman numbers indicate the expression in eq. (7). b_1 (bonds) and s_1 (sites) denote the sizes of the smallest pore elements, whereas b_2 (bonds) and s_2 (sites) correspond to the sizes of the largest pore elements

Pore Size Segregation Effect

One of the original contributions of the DSBM lies in its simple and systematic description of the size correlation among neighbouring pore components. Several methods for constructing porous networks have followed the principles of the DSBM [28-31]. However, the porous networks with the maximum randomness and isotropy among neighbouring sites and bonds can be constructed using the method find in [29] which is

J. Mex. Chem. Soc. **2024**, *68*(4)
Special Issue

ISSN-e 2594-0317

referred as the Pure MC method, inspired by the Monte Carlo sampling method of the NVT ensemble. This method involves randomly assigning sizes R_B and R_S from fixed functions $F_B(R_B)$ and $F_S(R_S)$, respectively, to bonds and sites of a given lattice. Subsequently, one Monte Carlo step is carried out executing N transitions (where N is equal to the total number of sites and bonds of the porous network). These transitions involve the interchange of sizes of two randomly chosen sites or two randomly chosen bonds in the lattice, according to the associated transition probabilities defined by the Metropolis algorithm [32,33]. The Monte Carlo steps are repeated until all the sites of the pore network satisfy the CP. The topology of pore networks obtained with this construction method is depicted in Fig. 4 [34], where three porous networks with $C = 4$ and different values are presented. In this figure, three sizes of sites are presented: small, medium, and large; the intervals of R_S, match these classifications by equalizing three areas below F_S. This figure illustrates two extreme cases and one that lies midway between them. The first extreme case corresponds to porous networks with $\Omega \to 0$ (see Fig. 4**(a)**); in this case, the size of the three domains formed with sites of similar sizes is quite small, and they are spatially distributed at random. The intermediate case is depicted in Fig. 4**(b)**, where $\Omega \approx 0.7$; the three domains possess a size that is neither too large nor too small, but rather intermediate. Finally, the second extreme case is represented for the condition $\Omega \to 1$, (see Fig. 4**(c)**); in this instance, the domains have a large size and are distributed evenly in all directions.

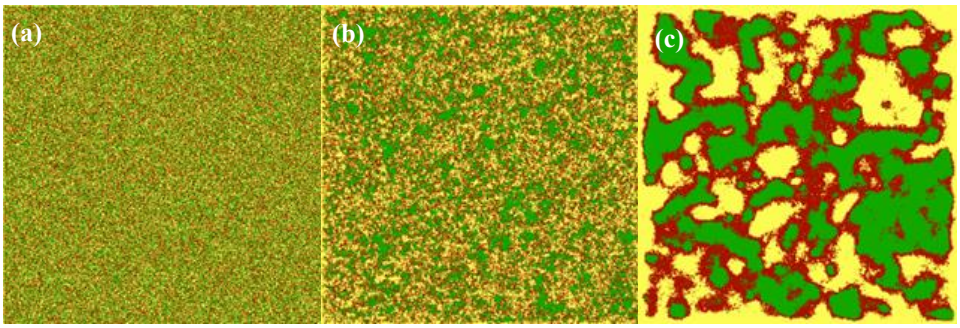

Fig. 4. Illustration depicting the spatial arrangement of domains within square porous networks, where each domain consists of sites of comparable size. The networks are characterized by $C = 4$ and a length of 100 nodes. Every pixel corresponds to a single site. Panel **(a)** $\Omega = 0.31$, panel **(b)** $\Omega = 0.68$, and panel **(c)** $\Omega = 0.92$. Sites of small, medium, and large sizes are represented by the colors green, red, and yellow, respectively.

Domains with uniformly sized sites can be described using a correlation length, which quantifies the size of regions within a porous network where the sites are strongly interrelated. This quantity is linked to the correlation function *C(r)*, which represents the relationship of site sizes in the vicinity of surrounding locations and is defined as follows,

$$C(r) = \frac{\langle (R_i - \overline{R}_S)(R_j - \overline{R}_S) \rangle}{\left[\langle (R_i - \overline{R}_S) \rangle^2 \, \langle (R_j - \overline{R}_S) \rangle^2 \right]^{1/2}} \tag{8}$$

where R_i and R_j are two sites separated by r lattice positions, and $\overline{R}_S$ is the medium size of R_S. Then, if $r = 1$, R_i and R_j are connected to the same bond. The relation between the correlation length ξ and C(r), goes as, [35,36]

$$C(r) = exp\left(-\frac{r}{\xi}\right) \tag{9}$$

J. Mex. Chem. Soc. **2024**, *68*(4)
Special Issue

ISSN-e 2594-0317

Fig. 5 presents a graph of ξ, as a function of Ω calculated through Eq. (9) for pore networks with C = 4 and different values of Ω. This figure suggests two things. First, the size of the domains with sites of similar sizes have a typical value of $\xi \to 0$ for $\Omega \to 0$, $\xi \to 3$ for $\Omega \approx 0.7$, and $\xi \to \infty$, for $\Omega \to 1$. A comparative analysis of Figs. 4 and 5 can be insightful for understanding the relationship between the values of ξ and the dimensions of the domains, especially considering the nearly identical sizes of the sites involved. And second, ξ is a function of Ω. The variation of ξ in relation to Ω can be interpreted physically in the following manner. Pore cavities of comparable dimensions aggregate into domains, the size of which changes in direct proportion to the Ω value. This grouping of pores into domains based on size allows for a structured categorization, reflecting the influence of Ω on the spatial distribution within the material.

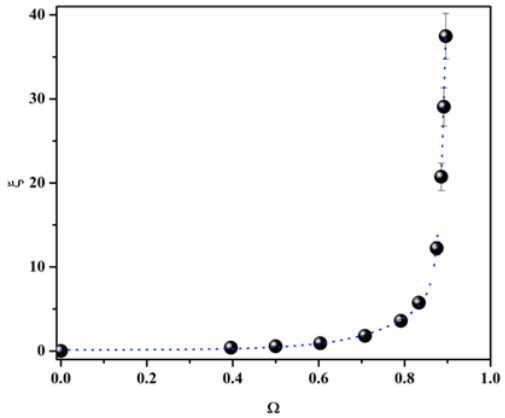

Fig. 5. Representation of the correlation length ξ as a function of Ω for pore networks with $C = 4$ and uniform distribution functions F_B and F_S [37].

Refinements of the DSBM

The DSBM, as outlined previously, is inadequate for characterizing the internal structure of materials lacking a porous network texture. This model does not account for the complexities of materials without such geometries, such as MCM-41 or SBA-15 materials, which are characterized by their pores arranged in a hexagonal cylindrical array. In the context of the DSBM framework, the model was enhanced by two key modifications: the inclusion of spatial interference between bonds and the introduction of variable connectivity.

Geometric interference of bonds

The early 1990s witnessed the advent of advanced materials such as MCM-41, SBA-15, and SBA-16, among others, signifying a significant development in the field of material sciences. [4]. These solid materials feature organized structures, which facilitates the accurate determination of pore sizes. The DSBM sought to describe structured materials by integrating suitable enhancements, maintaining its straightforwardness. This involved examining the alterations in the texture of porous networks that occur when the geometric interference of bonds converging at a single site is prevented [38]. Fig. 6 illustrates this concept.

J. Mex. Chem. Soc. **2024**, *68*(4)
Special Issue

ISSN-e 2594-0317

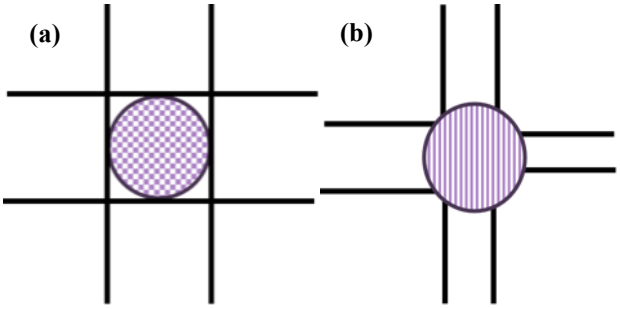

Fig. 6. Geometrical interference of four bonds converging the same site. Panel **(a)**, the sizes of the bonds are sufficiently large to cause mutual interference. Panel **(b)**, the sizes of the bonds are sufficiently minimal to prevent any mutual interference.

This last figure shows two scenarios involving four bonds connected to a single site on a square lattice. In Fig. 6**(a)**, geometrical interference occurs among the bonds, with the four bonds of equivalent size as the site itself. As a result, the site losses its circular geometry. Fig. 6**(b)**, illustrates four bonds converging the same site without overlapping. This last configuration maintains the site circular shape of the site and ensures that the bonds do not obstruct one another. Then, if the sites of the networks have to keep its cavity geometry, the elements of the pore network have to be linked with a CP different than previously defined. It should be noted that geometric interference may not be applicable to all porous materials being studied. The significance of these limitations can vary depending on the specific characteristics and applications of the material in question. Therefore, it is essential to evaluate the relevance of geometric restrictions on a case-by-case basis. For instance, the pores in plate-like materials do not interfere with each other; in this case the Hele-Shaw cells (spaces between rugged-parallel plates) [39] would describe much better the proper linkage among pores. Graphically, the size of any pair of bonds orthogonally connected to one site of size R_S on a square lattice, and subjected to geometrical restrictions, must fall within the area bounded by a circle of radius R_S and two perpendicular axis intersecting at the center of the circle, as depicted in Fig. 7. This area is defined as the incumbent volume of a site of size R_S when connected to two perpendicular bonds of sizes R_{B_1} and R_{B_2}.

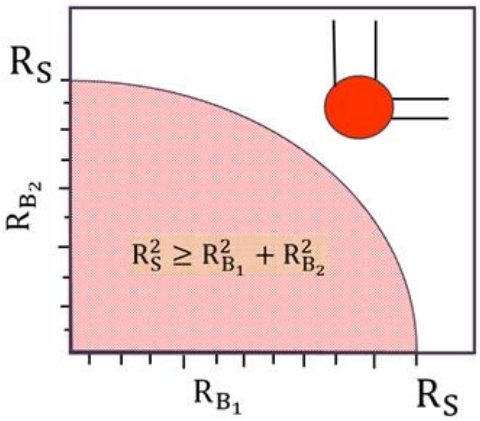

Fig. 7. Permitted sizes of two bonds orthogonally connected to one site. Any point located in the red area (incumbent volume of the site R_S) do not interfere with each other.

J. Mex. Chem. Soc. **2024**, *68*(4)
Special Issue

ISSN-e 2594-0317

The updating of the firs law that guarantee the fulfilment of geometric restrictions among the components of a porous network, is as follows,

$$B_C(R_S) \geq S(R_S), \quad \forall R_S \tag{10}$$

where $B_C(R_S)$ represents the fraction of bonds of size R_S or smaller that lie in the incumbent volume of sites smaller than or equal to R_S. The general expression for $B_C(R_S)$ can be articulated through the following equation (the integral boundaries are defined according to the type of lattice involved.) [40],

$$B_C(R_S) = \left\{ \int_0^{R_S} \cdots \int_0^{\square} F_B\left(R_{B_1}\right) \cdots F_B\left(R_{B_C}\right) dR_{B_1} \cdots dR_{B_C} \right\}^{1/C} \tag{11}$$

where $R_{B_1}, R_{B_2} \ldots R_{B_C}$ are the sizes of the *C*-connected bonds of sites of sizes R_S and $F_B\left(R_{B_1}\right) \cdots F_B\left(R_{B_C}\right)$ are the corresponding density functions of these bonds. For their part, the probability density function for the joint event of having a site of size R_S connected to bonds of sizes $R_{B_1} \cdots R_{B_C}$, is represented as follows,

$$\rho\left(R_S \cap R_{B_1} \cdots R_{B_C}\right) = F_S(R_S) F_B\left(R_{B_1}\right) \cdots F_B\left(R_{B_C}\right) \phi\left(R_S, R_{B_1} \cdots R_{B_C}\right) \tag{12}$$

Then, the updating of the second law can be written as,

$$\phi\left(R_S, R_{B_1} \cdots R_{B_C}\right) = 0, \quad \text{outside the incumbent volume} \tag{13}$$

where the expression of the correlation function changes as follows [40],

$$\phi\left(R_S, R_{B_1} \cdots R_{B_C}\right) = \frac{exp\left(-\int_{B_C(R_C)}^{B_C(R_S)} \frac{dB_C}{B_C - S}\right)}{B_C(R_C) - S(R_C)} \tag{14}$$

where R_c is the minimal size of a site that accommodates the precise set of $R_{B_1} \cdots R_{B_C}$bonds without geometric interference. The revised version of the CP is presented as follows: "While every bond converging into a site must be smaller in size than this last cavity, a pair of adjacent bonds converging to the site have still to assume the right combination of sizes to prevent any physical interference between them before meeting together into the site" [38,42].

Variable connectivity

To integrate variable connectivity one can introduce the notion of "virtual (closed) bonds" within a porous network that maintains a constant connectivity C_m [38, 41]. Refer to Fig. 8, which illustrates the sites of a square network with $C_m = 4$, connected to "virtual bonds".

J. Mex. Chem. Soc. **2024**, *68*(4)
Special Issue

ISSN-e 2594-0317

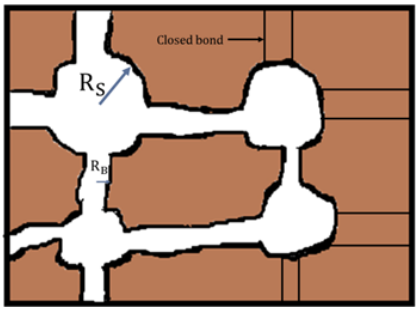

Fig. 8. Representation of the concept of virtual or closed bonds of sites of a square network with $C = 4$. The solid phase is represented in brown color.

Physically, "virtual bonds" represent the solid phase; mathematically, their size corresponds to $R_B = 0$. Then, the local connectivity of any *i*-site (C_i) is given by,

$$C_i = C_m - C_{i,0}, \quad \forall i \tag{15}$$

where $C_{i,0}$ is the number of virtual bonds of the *i*-site. If the average of C_i is calculated in the last equation, the average connectivity of the porous network ($\overline{C}$) is obtained,

$$\overline{C} = C_m(1 - f_0) \tag{16}$$

where f_0 stands for the fraction of closed bonds in the porous network. Taking into account the definition of closed bonds, F_B is redefined as follows,

$$F_B(R_B) = \begin{cases} f_0, & \text{for} \quad R_B = 0 \\ F'_B(R_B), & \text{for} \quad R_B > 0 \end{cases} \tag{17}$$

This last definition for F_B makes Eqs. (1)-(6) still valid. The following normalization condition holds,

$$\int_0^\infty F'_B(R_B) dR_B = 1 - f_0 \tag{18}$$

Fig. 9 shows the graphical representation of F_B and F_S for porous networks with variable connectivity.

J. Mex. Chem. Soc. **2024**, *68*(4)
Special Issue

ISSN-e 2594-0317

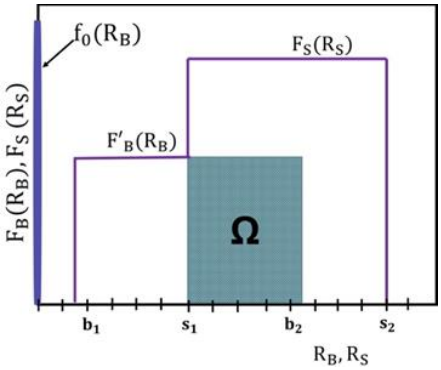

Fig. 9. Representation of the density functions F_B and F_S for porous networks with variable connectivity.

Correlated Networks with geometric restrictions and variable connectivity

The interplay of variable connectivity and geometric restriction of bonds results in the formation of porous networks exhibiting simultaneous segregation based on size and connectivity when the density functions F_B and F_S overlap [42]. Throughout the 2010s, the AAPS introduced a variety of advanced computational techniques for the development of porous network structures. These innovative methods have significantly contributed to the field, offering new insights and approaches to the construction of these complex systems [30,38, 43 - 45]. Refer to Fig. 10 to observe the simultaneous effects of size and connectivity segregation. This figure presents visual representations of central sections of porous networks with $\overline{C} = 4$ and different values of $\xi(0.94,3.0,9.0)$; it is organized into two columns. The top row displays central planes representing the spatial distribution of sites in three sizes: small, medium, and large. The bottom row shows color-coded central sections, which illustrate the spatial arrangement of site connectivity. In the image, orange pixels represent sites where $C_i = 1,2$. Sites with $C_i = 3,4$ are indicated by blue pixels. Finally, gray pixels denote sites with $C_i = 5,6$. Each column in this figure corresponds to the same porous network: the first column, from left to right, corresponds to $\xi = 0.94$; the second column to $\xi = 3.0$; and the third column to $\xi = 9.0$.

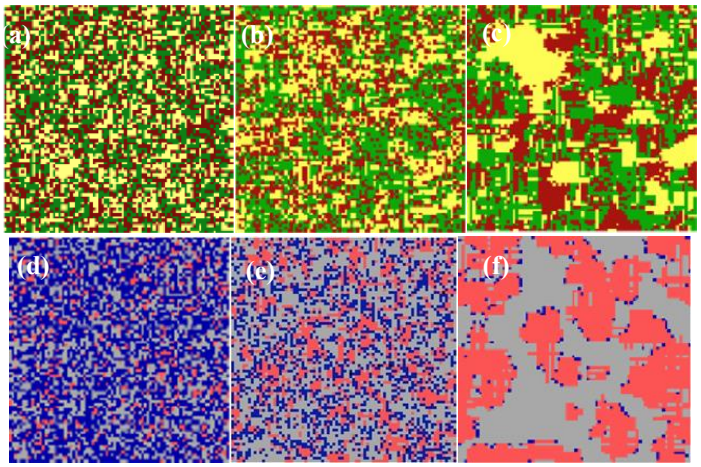

Fig. 10. Schematization of the spatial distribution of the connectivity and sizes of sites on cubic porous networks with $\overline{C} = 4$ and a length of 100 nodes. **(a)**, **(d)** $\xi = 0.94$. **(b)**, **(e)** $\xi = 3.0$. **(c)**, **(f)** $\xi = 9.0$. Top row represents sizes of sites: green (small), red (medium), yellow(large). Bottom row stands for local connectivity of sites: orange $C_i = 1,2$. Blue $C_i = 3,4$. Gray $C_i = 5,6$. Each pixel represents one site. Each image corresponds to middle planes of cubic porous networks.

J. Mex. Chem. Soc. **2024**, *68*(4)
Special Issue

ISSN-e 2594-0317

Fig. 10 is described as follows. As $\xi \to 0$, the sizes and local connectivity of sites become randomly assorted throughout the space; see Figs. 10**(a)** and 10**(d)**. This situation corresponds to distributions F_B and F_S being sufficiently separated on a graph, allowing every site within F_S to accommodate any combination of $R_{B_1} \cdots R_{B_C}$ bonds without any geometric interference. Yet, when $\xi > 1$, the sizes of adjacent sites become increasingly alike, leading to the formation of distinctive domains with a typical size ξ, as illustrated in Fig. 10**(b)**. This phenomenon is completely equivalent to what has been outlined in preceding sections. However, the novel aspect highlighted is the effect of connectivity segregation, as depicted in Fig. 10**(e)**. This phenomenon involves the clustering of sites that share comparable values of local connectivity. In Fig. 10**(e)**, adjacent sites are spatially organized based on their C_i values. The sites with C_i values of 5 and 6, those with 3 and 4, and those with 1 and 2, are each clustered into separate, cohesive domains. These domains are visually differentiated by gray, blue, and orange colors, respectively. When the parameter ξ significantly exceeds 1, the structure of the porous networks transitions into configurations predominantly characterized by two major connectivity domains. Specifically, one domain exhibits local connectivity C_i of either 1 or 2, whereas the other domain is distinguished by higher C_i values to 5 or 6, as depicted in Fig. 10**(f)**. These domains are separated by a dispersed interface composed of sites with C_i 3 or 4. The observed phenomenon arises from the distributions of F_B and F_S, particularly when the variable ξ attains its peak value in relation to the network's average connectivity. Geometric interference indicates that the best approach is to connect the smallest feasible site capable of supporting a sequence of bonds $R_{B1}...R_{BC}$ of the largest dimensions, thereby achieving a local connectivity of C_i=5 or 6. In contrast, larger sites should be linked to bonds of similar size. This approach is practical when these bonds are classified by F_B as large and the sites demonstrate a local connectivity of C_i=1 or 2, with their respective C_i-bonds situated on directly opposite sides of the site. To complement Fig. 10, Fig. 11 presents drawings of the domains. These domains in Fig. 11 are characterized by alternating sites of high and low local connectivity, providing a visual representation of the spatial distribution of connectivity values within the domain. This illustration highlights the contrast and interplay between regions of differing connectivity levels.

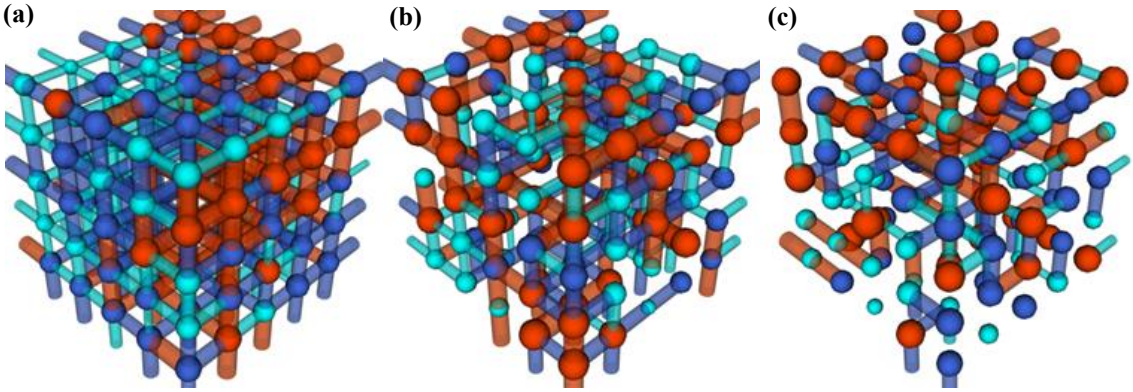

Fig. 11. Cubic networks with a high correlation are structured into regions measuring 5x5x5. (a) $\overline{C} = 6$. (b) $\overline{C} = 4$. (c) $\overline{C} = 2$. Colors are utilized to create a contrast.

Interpretation of N_2 isotherms through correlated Porous Networks

Assumptions

The straightforward geometry of porous networks enables a useful qualitative analysis of the shape of the boundary curves (both ascending and descending) and the Primary Ascending and Descending Scanning Curves of N_2 isotherms, based on the sizes, geometry, and interconnection among porous entities. The pore

J. Mex. Chem. Soc. **2024**, *68*(4)
Special Issue

ISSN-e 2594-0317

volume of sites and bonds can be controlled by establishing a suitable distance from the node (center of each site) to the node of the porous network. To obtain N_2 isotherms, the following rough assumptions are made for the adsorption processes (whether boundary or primary ascending curve).

I. During adsorption, as the pressure of the adsorbing gas increases, an adsorbed layer, denoted by thickness t, progressively forms on the surface of sites and bonds. The value of t can be calculated using a suitable equation, such as the Halsey-type equation [46].
II. The adsorbed layer on each site and bond reaches a limit value at a certain pressure, imposed by the balance between the mechanical equilibrium of the adsorbed phase and the physical attraction of the pore walls. The classical Kelvin equation provides a corresponding radius of curvature, R_C, that defines the porous elements ready to condensate, written as,

$$R_C = \frac{2\sigma^{lv}v^l}{R_g T ln(p/p^0)} \tag{19}$$

where R_g is the gas constant, T is the absolute temperature, σ^{lv} is the interfacial tension between liquid and vapor phases, p is the gas bulk pressure, p_0 is the saturation pressure defined by T, and v^l is the molar volume of the liquid phase of the adsorptive.

III. The condition for the onset of capillary condensation is given by $(R_B - t) \leq R_C/2$. However, if at least one of its two neighboring sites of the bonds is already filled with condensate, they acquire a hemispherical interface at one of its ends. This could trigger the advancement of the meniscus to the other end of the bond if it also fulfills the condition $R_C/2 \leq (R_B - t) \leq R_C$. This latter mechanism of condensation is a cooperative effect known as advanced adsorption [47]
IV. As for sites, they develop a continuous hemispherical liquid-vapor interface if either all of their C bonds or at least C-1 bonds are already occupied with condensate. Then, if this condition is satisfied, and also $(R_S - t) \leq R_C$, the sites are immediately occupied by condensate. On the other hand, the following suppositions are assumed for the desorption processes (either boundary or primary descending curve).
V. Occupied pores (sites or bonds) with condensate can evaporate if they have reached the condition $R_B \geq R_C$ or $R_S \geq R_C$, and if there exists a liquid-vapor interface at their junctions that promotes the development of evaporation of the pore entity. The latter condition is met if exists a pathway from the evaporating pore to the bulk vapor phase (for the boundary descending curve) or at least one of its connected pores have not been filled with condensate (primary descending curve). Thus, desorption is controlled by the classical pore-blocking effect [48,49] and the percolation phenomenon.
VI. Once a pore entity is emptied, as the pressure steadily declines, the thickness of the adsorbed layer correspondingly diminishes.

It is important to note that the suppositions outlined above do not allow for an accurate assessment of the shape of the isotherms. Detailed molecular simulation methods have shown that the form of the isotherms is influenced by the trajectory over a landscape of metastable states of the thermodynamic potential, which is influenced by the detailed molecular configurations of the adsorbed gas molecules and the microscopic characteristics of the surface of the pore walls [50].

Consequently, these suppositions are not capable of describing phenomena such as cavitation, which results from molecular fluctuations of the adsorbed phase [51,52]. Nevertheless, the N_2 isotherms of networks constructed under the framework of the DSBM have proven to be a very useful tool, providing a simple framework for qualitatively interpreting the appearances of boundary curves (ascending or descending) and primary scanning curves (ascending or descending) [53]. This is described next.

Figs. 12 and 13 provide a summary of poorly correlated and highly correlated N_2 isotherms at 77 K, depicting porous networks with diverse mean connectivity values. It is evident from these figures that the

J. Mex. Chem. Soc. **2024**, *68*(4)
Special Issue

ISSN-e 2594-0317

appearance of the boundary curves cannot be strictly classified as types H1, H2, or H3 of the original IUPAC classification of sorption hysteresis loops [48], although they exhibit hybrid shapes with different degrees of these IUPAC types, depicted in Fig.14. In broad terms, networks with $\Omega = 0$ (left columns of Figs. 12 and 13) are typically associated with H1 loops, though a transition to H2 types occurs if the volume of bonds significantly exceeds the volume of sites [53]. In contrast, highly correlated porous networks (right columns of Figs. 12 and 13) yield cycles with sloping ascending and descending boundary curves, representing hybrids between H1 and H3 loops.

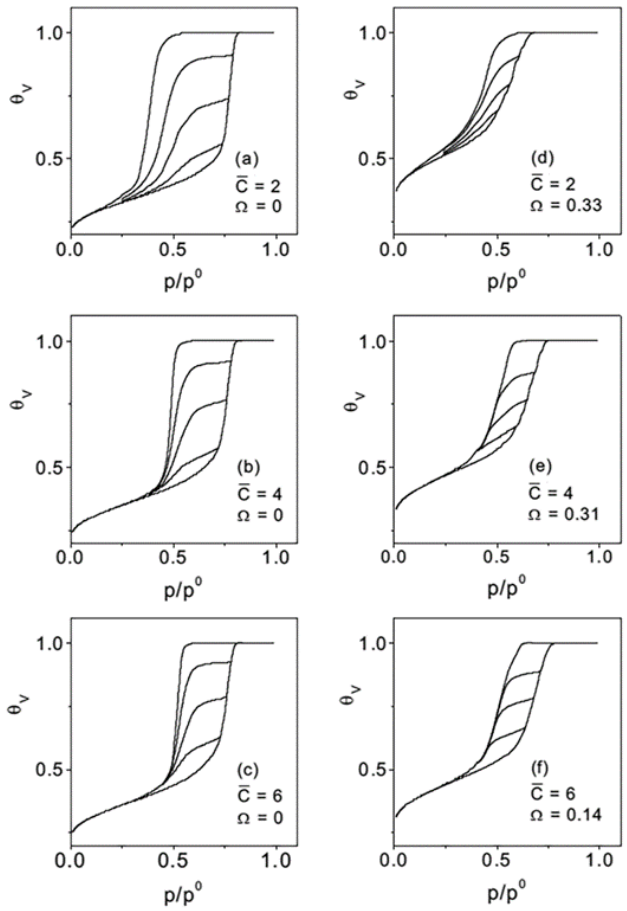

Fig. 12. Simulated nitrogen sorption isotherms at 77 K on porous networks. In this figure, θ_v represents the degree of filling of the porous network with adsorbate, while p represents the gas bulk pressure, and p_0 is the saturation pressure. The adsorption hysteresis loops are organized according to $\overline{C}$ and Ω. Sets of primary descending curves are included. Reproduced from [53] with permission from the Royal Society of Chemistry.

J. Mex. Chem. Soc. **2024**, *68*(4)
Special Issue

ISSN-e 2594-0317

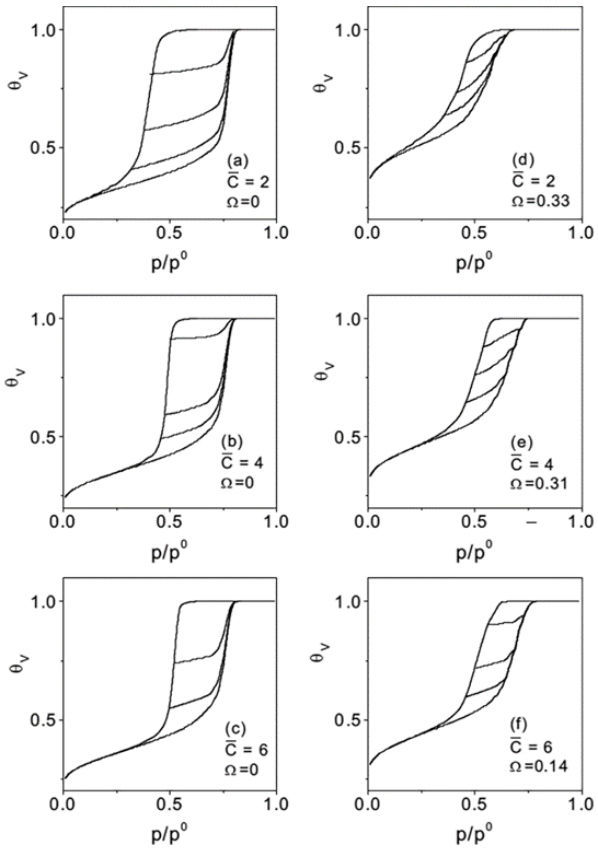

Fig. 13. Simulated nitrogen sorption isotherms at 77 K on porous networks. In this figure, θ_v represents the degree of filling of the porous network with adsorbate, while p represents the gas bulk pressure, and p_0 is the saturation pressure. The adsorption hysteresis loops are organized according to $\overline{C}$ and Ω. Sets of primary ascending curves are included. Reproduced from [53] with permission from the Royal Society of Chemistry.

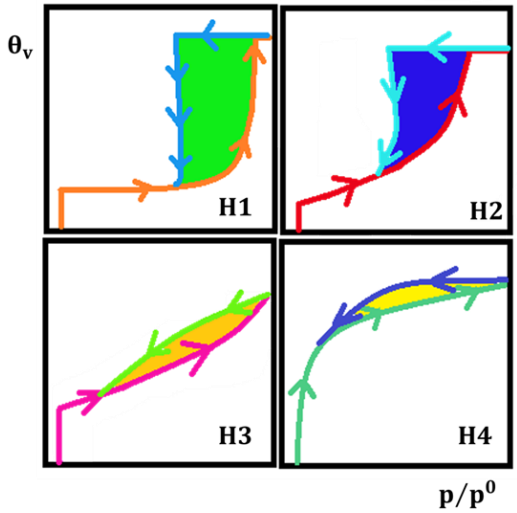

Fig. 14. Diagrammatic illustration of the original IUPAC categorization for sorption hysteresis loops [48].

J. Mex. Chem. Soc. **2024**, *68*(4)
Special Issue

ISSN-e 2594-0317

Adsorption and desorption in poorly correlated (Ω=0) porous networks

In order to understand the shapes of the boundary curves of the isotherms in Figs. 12 and 13, the concept of multiplex (independent domain) must be introduced. A multiplex is a unit cell consisting of a site and its C-half bonds (half, because one bond is shared with two sites). See Fig. 15. This multiplex can condensate and evaporate without networking effects, because it is assumed that each one maintains immediate contact with the bulk phase of the adsorbing gas. If the algorithm to simulate N_2 adsorption, described in the previous section, is applied to the set of multiplexes that comprise each porous network in Figs. 12 and 13, we obtain the set of isotherms presented in Fig. 16.

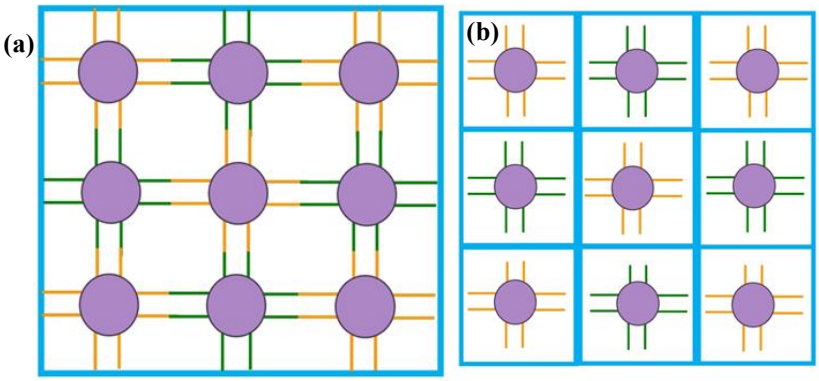

Fig. 15. (a) Visual representation of a porous network, and **(b)** the concept of multiplex.

From the last figure, it is observed that the ascending boundary curves of poorly correlated networks (left column of Fig. 13) practically coincides with those of the multiplex´s isotherms in Fig. 16 (left column). However, the descending boundary curves of these uncorrelated porous networks differ considerably from those of the multiplexes. The coincidence of the ascending boundary curves of networks and multiplexes can be explained by the significant difference in sizes between connected sites and each of their C-bonds. This difference of sizes implies that the pressure required for filling the bonds is small enough compared to the pressure needed for the filling their connected sites. Consequently, when the sites are ready to be occupied with condensate at certain pressure, almost all of their connected bonds are already occupied with condensate. This suggests that for poorly correlated networks, it is possible to accurately calculate the pore size distribution of sites using the ascending boundary curves when the volume of sites is considerably greater than that of the bonds, or the pore size distribution of bonds when the volume of bonds is considerably greater than that of the bonds [53]. As for the descending boundary curves of poorly correlated networks, the great difference between the curves of networks and multiplexes can be entirely explained by percolating phenomenon. This phenomenon states that the position of the knee in the descending boundary curves is influenced by the value of the mean connectivity $\overline{C}$ [54]. This is due to the almost random spatial distribution of sizes of bonds throughout each of the uncorrelated porous networks. Another consequence of this is the challenge in deducing the distribution of pore sizes among sites or bonds from the boundary desorption curves, given the concurrent occurrence of the classical pore blocking effect and the percolation phenomenon.

J. Mex. Chem. Soc. **2024**, *68*(4)
Special Issue

ISSN-e 2594-0317

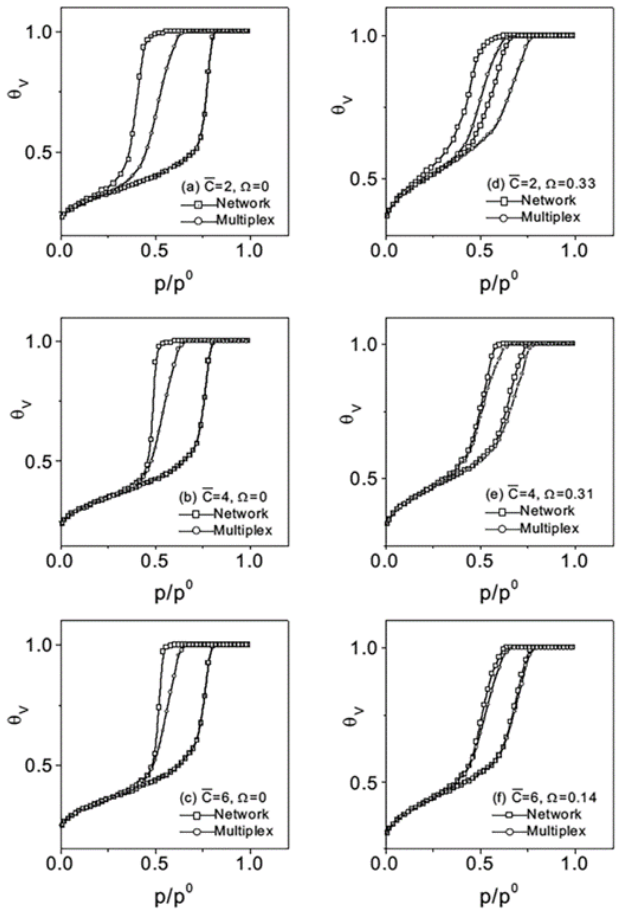

Fig. 16. Comparison of isotherms between porous networks and sorption curves obtained with multiplexes. Both structures possess the same pore-size distributions. Reproduced from [53] with permission from the Royal Society of Chemistry.

Adsorption and desorption in highly correlated porous networks

For highly correlated porous networks, the shapes of their loops are associated with hybrid types between the H1 and H3 classification (right columns of figures 12 and 13). To quantify the extent of cooperative effects during the course of the boundary curves, a comparison must be made with the isotherms of the independent domains (multiplexes) through Fig. 16 (right column). In this way, the cooperative effects due to the advancement of hemispherical meniscus through the ends of bonds increase as the mean connectivity, $\overline{C}$ decreases. While it is almost absent for porous network with $\overline{C} = 6$ (check out the coincidence between the ascending boundary curves of the network and the one of the multiplexes; Fig. 16, bottom right column), it is very strong for the porous network with $\overline{C} = 2$ (note the strong divergence between the ascending boundary curves between the porous network and that one of multiplexes; Fig. 16, top right column). The observed phenomenon can be attributed to the significant correlation between the sizes within the porous network and the average value of $\overline{C}$, which is 2. This network comprises an array of elongated cylindrical capillaries, each featuring a variable cross-sectional area. The larger sections correspond to the sites, while the narrower sections

J. Mex. Chem. Soc. **2024**, *68*(4)
Special Issue

ISSN-e 2594-0317

represent the bonds. These long capillaries are connected among them through the connection of sites with $\overline{C} > 3$, which act as manifold capillary distributors. Then, once a small enough bond (minimum of a cross-sectional area of a long capillary) fills independently with condensate, at its corresponding value of pressure, immediate condensation occurs in their two connected sites (given the similar size among them), which then triggers the advancement of the hemispherical meniscus throughout the whole structure of the long capillary. On the other hand, porous network with $\overline{C} = 6$ are composed of domains with sites with very similar sizes connected through bonds with also very similar sizes among them, but considerably smaller, due to the geometrical restriction, than those of the sites of the domain. This difference in size between R_B and R_s in each domain promotes the independent condensation of bonds and sites at each value of pressure during the course of the ascending boundary curve. Then for this porous network, the ascending boundary curve can be depicted as a succession of orderly of filling of independent domains according to the size of sites and bonds, from small pore domains at the beginning of the curve to large pore domains at the onset of the ascending boundary curve. The cooperative effects during the course of the ascending boundary curve for porous network with $\overline{C} = 4$ are intermediate between the cases for $\overline{C} = 2$ and $\overline{C} = 6$.

The boundary curves delineating highly correlated porous networks exhibit a less pronounced descent compared to those of uncorrelated structures. Additionally, the knees of these curves appear at higher pressure values when contrasted with an uncorrelated porous network possessing an equivalent mean connectivity. This phenomenon can be elucidated by examining percolation in correlated lattices. Research indicates that an increase in the correlation length leads to a lower percolation threshold. Essentially, as the degree of correlation intensifies, it becomes easier for a network to reach a state of percolation, facilitating the process at a quicker rate [55, 56]. Then, the boundary descent curves of each porous network differ from the corresponding multiplex. This mismatch is significantly greater in the case of $\overline{C} = 2$ (Fig. 16, top right column), while it is moderate for $\overline{C} = 4$,(Fi. 16, middle right column) and nearly non-existent for $\overline{C} = 6$ (Fig. 16, bottom right column). The strong correlation observed between the network and multiplexes' isotherms, particularly in highly interconnected porous networks with an average connectivity of 6, indicates that assuming an accurate meniscus geometry can yield precise calculations of pore size distribution. This is crucial for analyzing the ascending or descending parts of boundary curves. Such insights are essential for characterizing and analyzing porosity and pore structures [53].

Primary ascending and descending scanning curves

The primary ascending and descending scanning curves of the isotherms indicate the existence of pore domains that behave either independently or in a connected manner. [56]. In this analysis, the primary scanning curves of the weakly correlated networks, as shown in the left columns of Figs. 12 and 13, tend to approach the lower (for descending scanning curves) or upper (for ascending scanning curves) endpoints of the corresponding hysteresis loop. This convergence suggests the existence of interconnected pore domain behaviour, specifically the pore blocking phenomenon. This description is also relevant for a highly correlated porous network where the average mean connectivity is 2. The isotherms in the top right of Figs. 12 and 13 illustrate this, as they are influenced by significant cooperative effects during adsorption and pore blocking phenomena during desorption. In turn, when examining the primary ascending and descending scanning curves of highly correlated structures, it is intriguing to note that for structures with intermediate and low medium connectivity, these curves tend to converge towards the boundary curve within a narrow pressure range. This merging is clearly observed in isotherms e and f, as illustrated in Figs. 12 and 13. These figures suggest a nearly flat line ($\overline{C} = 6$) or a gently sloping curve ($\overline{C} = 4$) intersecting the corresponding boundary curves. It is significant to recognize that the specific patterns of the primary descending scanning curves in a highly correlated porous network, characterized

J. Mex. Chem. Soc. **2024**, *68*(4)
Special Issue

ISSN-e 2594-0317

by an average connectivity of 2, provided a framework for the AAPS to conduct experimental studies on the cooperative phenomena observed in undulated SBA-15 materials. [57].

Conclusions

The Academic Area of Physicochemical Surfaces has significantly advanced the field by introducing the DSBM, a model that simplifies the understanding of porous materials' texture and their nitrogen sorption properties. Utilizing dual pore size distributions for sites and bonds, the DSBM aids in constructing a theoretical framework of porosity, connecting diverse porous structures. This model enables the analysis of porous topologies by examining the dimensions and interconnectivity of adjacent pore elements. Notably, the correlation length within the DSBM is crucial for identifying domains with similarly sized pores. As a tool, the DSBM is pivotal in deciphering complex patterns in sorption data, illuminating the spatial arrangement of pores and their connections within a solid matrix. This is achieved through qualitative examination of nitrogen adsorption curve shapes and their association with cooperative behaviors during adsorption and desorption processes. While fully characterizing a porous solid's texture from gas sorption remains elusive, the DSBM offers a comprehensive guide for interpreting experimental outcomes by qualitatively assessing the boundary curves and primary scanning curves.

Acknowledgements

A.L.T.G. acknowledges the financial support through the scholarship CONAHCyT (Grant No. 794571 and 64f687d78ec4c663f15b663c). V.M.T acknowledges the financial support provided by Conahcyt through the program “Convocatoria Ciencia Básica y de Frontera 2023-2024,” grant number CBF2023-2024-2725.

References

1. Tovbin, Yu. K. The Molecular Theory of Adsorption in Porous Solids, 1st ed.; CRC Press, **2017**. DOI: https://doi.org/10.1201/9781315116297.
2. Ghanbari, T.; Abnisa, F.; Wan Daud, W. M. A. A Review on Production of Metal Organic Frameworks (MOF) for CO2 Adsorption. *Science of The Total Environment* **2020**, *707*, 135090. DOI: https://doi.org/10.1016/j.scitotenv.2019.135090.
3. Verma, P.; Kuwahara, Y.; Mori, K.; Raja, R.; Yamashita, H. Functionalized Mesoporous SBA-15 Silica: Recent Trends and Catalytic Applications. *Nanoscale* **2020**, *12*, 11333–11363. DOI: https://doi.org/10.1039/D0NR00732C.
4. Characterization of Porous Solids and Powders: Surface Area, Pore Size and Density, [4. ed.], 1. repr. with some corr.; Lowell, S., Ed.; Particle technology series; Springer: Dordrecht, **2010**.
5. Brunauer, S.; Emmett, P. H.; Teller, E. Adsorption of Gases in Multimolecular Layers. *J. Am. Chem. Soc.* **1938**, *60*, 309–319. DOI: https://doi.org/10.1021/ja01269a023.
6. Naderi, M. Chapter Fourteen - Surface Area: Brunauer–Emmett–Teller (BET). In Progress in Filtration and Separation; Tarleton, S., Ed.; Academic Press: Oxford, **2015**; pp 585–608. DOI: https://doi.org/10.1016/B978-0-12-384746-1.00014-8.
7. Wu, J.; Li, Z. Density-Functional Theory for Complex Fluids. Annu. Rev. Phys. Chem. **2007**, 58, 85–112. DOI: https://doi.org/10.1146/annurev.physchem.58.032806.104650.
8. Wu, J. Density Functional Theory for Chemical Engineering: From Capillarity to Soft Materials. *AIChE Journal* **2006**, *52*, 1169–1193. DOI: https://doi.org/10.1002/aic.10713.
9. Makkar, P.; Ghosh, N. N. A Review on the Use of DFT for the Prediction of the Properties of Nanomaterials. *RSC Adv.* **2021**, *11*, 27897– 27924. DOI: https://doi.org/10.1039/D1RA04876G.

J. Mex. Chem. Soc. **2024**, *68*(4)
Special Issue

ISSN-e 2594-0317

10. Gubbins, K. E.; Sliwinska-Bartkowiak, M.; Suh, S.-H. Molecular Simulations of Phase Transitions in Pores. *Molecular Simulation* **1996**, *17*, 333– 367. DOI: https://doi.org/10.1080/08927029608024116.
11. Segura, C. J.; Vakarin, E. V.; Chapman, W. G.; Holovko, M. F. A Comparison of Density Functional and Integral Equation Theories vs Monte Carlo Simulations for Hard Sphere Associating Fluids near a Hard Wall. *The Journal of Chemical Physics* **1998**, *108*, 4837–4848. DOI: https://doi.org/10.1063/1.475893.
12. Zaragoza, A.; Gonzalez, M. A.; Joly, L.; López Montero, I.; Canales, M. A.; Benavides, A. L.; Valeriani, C. Molecular Dynamics Study of Nanoconfined TIP4P/2005 Water: How Confinement and Temperature Affect Diffusion and Viscosity. *Phys. Chem. Chem. Phys.* **2019**, *21*, 13653–13667. DOI: https://doi.org/10.1039/C9CP02485A.
13. Yuan, Z.; He, G.; Li, S. X.; Misra, R. P.; Strano, M. S.; Blankschtein, D. Gas Separations Using Nanoporous Atomically Thin Membranes: Recent Theoretical, Simulation, and Experimental Advances. *Advanced Materials* **2022**, *34*, 2201472. DOI: https://doi.org/10.1002/adma.202201472.
14. Yuan, Z.; Govind Rajan, A.; He, G.; Misra, R. P.; Strano, M. S.; Blankschtein, D. Predicting Gas Separation through Graphene Nanopore Ensembles with Realistic Pore Size Distributions. *ACS Nano* **2021**, *15*, 1727–1740. DOI: https://doi.org/10.1021/acsnano.0c09420.
15. Wang, Y.; Fan, Z.; Qian, P.; Ala-Nissila, T.; Caro, M. A. Structure and Pore Size Distribution in Nanoporous Carbon. *Chem. Mater.* **2022**, *34*, 617–628. DOI: https://doi.org/10.1021/acs.chemmater.1c03279.
16. Iftimie, R.; Minary, P.; Tuckerman, M. E. Ab Initio Molecular Dynamics: Concepts, Recent Developments, and Future Trends. *Proc. Natl. Acad. Sci. U.S.A.* **2005**, *102*, 6654–6659. DOI: https://doi.org/10.1073/pnas.0500193102.
17. Barrett, E. P.; Joyner, L. G.; Halenda, P. P. The Determination of Pore Volume and Area Distributions in Porous Substances. I. Computations from Nitrogen Isotherms. *J. Am. Chem. Soc.* **1951**, *73*, 373–380. DOI: https://doi.org/10.1021/ja01145a126.
18. Broekhoff, J. Studies on Pore Systems in Catalysts IX. Calculation of Pore Distributions from the Adsorption Branch of Nitrogen Sorption Isotherms in the Case of Open Cylindrical Pores A. Fundamental Equations. *Journal of Catalysis* **1967**, *9*, 8–14. DOI: https://doi.org/10.1016/0021-9517(67)90174-1.
19. Everett, D. H.; Haynes, J. M. Model Studies of Capillary Condensation. I. Cylindrical Pore Model with Zero Contact Angle. *Journal of Colloid and Interface Science* **1972**, *38*, 125–137. DOI: https://doi.org/10.1016/0021-9797(72)90228-7.
20. Feng, Q.; Xing, X.; Wang, S.; Liu, G.; Qin, Y.; Zhang, J. CO2 Diffusion in Shale Oil Based on Molecular Simulation and Pore Network Model. *Fuel* **2024**, *359*, 130332. DOI: https://doi.org/10.1016/j.fuel.2023.130332.
21. García-Salaberri, P. A.; Zenyuk, I. V. A General Purpose Tool for Modeling Multifunctional Thin Porous Media (POREnet): From Pore Network to Effective Property Tensors. Heliyon **2024**, *10*, e26253. DOI: https://doi.org/10.1016/j.heliyon.2024.e26253.
22. Söllner, J.; Neimark, A.; Thommes, M. Development and Application of an Advanced Percolation Model for Pore Network Characterization by Physical Adsorption. July 23, **2024**. DOI: https://doi.org/10.26434/chemrxiv-2024-h9zlm-v3.
23. A Model of Adsorption-Desorption Hysteresis in Which Hysteresis Is Primarily Developed by the Interconnections in a Network of Pores. *Proc. R. Soc. Lond. A* **1983**, *390*, 47–72. DOI: https://doi.org/10.1098/rspa.1983.0122.
24. Determination of the Pore-Size Distributions and Pore-Space Interconnectivity of Vycor Porous Glass from Adsorption-Desorption Hysteresis Capillary Condensation Isotherms. *Proc. R. Soc. Lond. A* **1988**, *415*, 453–486. DOI: https://doi.org/10.1098/rspa.1988.0023.
25. Neimark, A. V. Percolation Theory of Capillary Hysteresis Phenomena and Its Application for Characterization of Porous Solids. In Studies in Surface Science and Catalysis; Elsevier, **1991**; Vol. 62, pp 67–74. DOI: https://doi.org/10.1016/S0167-2991(08)61310-5.
26. Seaton, N. A. Determination of the Connectivity of Porous Solids from Nitrogen Sorption Measurements. *Chemical Engineering Science* **1991**, *46*, 1895–1909. DOI: https://doi.org/10.1016/0009-2509(91)80151-N.

J. Mex. Chem. Soc. **2024**, *68*(4)
Special Issue

ISSN-e 2594-0317

27. Mayagoitia, V.; Javier Cruz, M.; Rojas, F. Mechanistic Studies of Capillary Processes in Porous Media. Part 1.—Probabilistic Description of Porous Media. *J. Chem. Soc., Faraday Trans. 1* **1989**, *85*, 2071. DOI: https://doi.org/10.1039/f19898502071.
28. Mayagoitia, V.; Rojas, F.; Kornhauser, I.; Pérez Aguilar, H. Modeling of Porous Media and Surface Structures: Their True Essence as Networks. *Langmuir* **1997**, *13*, 1327–1331. DOI: https://doi.org/10.1021/la950812m.
29. Riccardo, J. L.; Steele, W. A.; Cuesta, A. J. R.; Zgrablich, G. Pure Monte Carlo Simulation of Model Heterogeneous Substrates: From Random Surfaces to Many-Site Correlations. *Langmuir* **1997**, *13*, 1064–1072. DOI: https://doi.org/10.1021/la9510036.
30. Román-Alonso, G.; Rojas-González, F.; Aguilar Cornejo, M.; Cordero-Sánchez, S.; Castro-García, M. A. In-Silico Simulation of Porous Media: Conception and Development of a Greedy Algorithm. *Microporous and Mesoporous Materials* **2011**, *137*, 18–31. DOI: https://doi.org/10.1016/j.micromeso.2010.08.016.
31. Riccardo, J. L.; Pereyra, V.; Zgrablich, G.; Rojas, F.; Mayagoitia, V.; Kornhauser, I. Characterization of Energetic Surface Heterogeneity by a Dual Site-Bond Model. *Langmuir* **1993**, *9*, 2730–2736. DOI: https://doi.org/10.1021/la00034a037.
32. Metropolis, N.; Rosenbluth, A. W.; Rosenbluth, M. N.; Teller, A. H.; Teller, E. Equation of State Calculations by Fast Computing Machines. *The Journal of Chemical Physics* **1953**, *21*, 1087– 1092. https://doi.org/10.1063/1.1699114.
33. Bhanot, G. The Metropolis Algorithm. *Rep. Prog. Phys.* **1988**, *51*, 429–457. DOI: https://doi.org/10.1088/0034-4885/51/3/003.
34. Cordero Sánchez, S. Simulación de redes porosas por métodos de Monte Carlo. Maestría en Ciencias, Universidad Autónoma Metropolitana, **1998**, p ht24wj79w. DOI: https://doi.org/10.24275/uami.ht24wj79w.
35. Sapag, K.; Bulnes, F.; Rizzotto, M.; Riccardo, J. L.; Zgrablich, G. On the Topology of Correlated Energies on Heterogeneous Surfaces. *J. Phys.: Condens. Matter* **1993**, *5*, A241–A242. https://doi.org/10.1088/0953-8984/5/33A/080.
36. Cruz, O.; Hidalgo, R.; Alas, S.; Cordero, S.; Meraz, L.; Lopez, R.; Dominguez, A. Is the Alexander–Orbach Conjecture Suitable for Treating Diffusion in Correlated Percolation Clusters? *Adsorption Science & Technology* **2011**, *29*, 663–676. DOI: https://doi.org/10.1260/0263-6174.29.7.663.
37. Tellez González, A. L. Estudio fractal de la reacción de oxidación de CO en Pt(100) por Monte Carlo. Maestría en Ciencias, Universidad Autónoma Metropolitana, Mexico City, **2022**.
38. Cordero-Sánchez, S.; Rojas-González, F.; Román-Alonso, G.; Castro-García, M. A.; Aguilar Cornejo, M.; Matadamas-Hernández, J. Pore Networks Subjected to Variable Connectivity and Geometrical Restrictions: A Simulation Employing a Multicore System. *Journal of Computational Science* **2016**, *16*, 177–189. DOI: https://doi.org/10.1016/j.jocs.2016.06.003.
39. Paterson, L. Radial Fingering in a Hele Shaw Cell. *J. Fluid Mech.* **1981**, *113*, 513. https://doi.org/10.1017/S0022112081003613.
40. Mayagoitia, V.; Rojas, F.; Kornhauser, I.; Zgrablich, G.; Faccio, R. J.; Gilot, B.; Guiglion, C. Refinements of the Twofold Description of Porous Media. *Langmuir* **1996**, *12*, 211–216. DOI: https://doi.org/10.1021/la940704k.
41. Ramirez-Cuesta, A. J.; Cordero, S.; Rojas, F.; Faccio, R. J.; Riccardo, J. L. On Modeling, Simulation and Statistical Properties of Realistic Three Dimensional Porous Networks. *Journal of Porous Materials* **2001**, *8*, 61–76. DOI: https://doi.org/10.1023/A:1026526502692.
42. Cordero, S.; Rojas, F.; Riccardo, J. L. Simulation of Three-Dimensional Porous Networks. *Colloids and Surfaces A: Physicochemical and Engineering Aspects* **2001**, *187–188*, 425–438. https://doi.org/10.1016/S0927-7757(01)00610-0.
43. Gonzalez Mendez, A.; Roman Alonso, G.; Rojas Gonzalez, F.; Castro Garcia, M. A.; Aguilar Cornejo, M.; Cordero Sanchez, S. Construction of Porous Networks Subjected to Geometric Restrictions by Using OpenMP. In 2014 IEEE International Parallel & Distributed Processing Symposium Workshops; IEEE: Phoenix, AZ, **2014**; pp 1189–1197. DOI: https://doi.org/10.1109/IPDPSW.2014.134.

J. Mex. Chem. Soc. **2024**, *68*(4)
Special Issue

ISSN-e 2594-0317

44. Matadamas, J.; Roman, G.; Rojas, F.; Castro, M.; Cordero, S.; Aguilar, M. Pore Network Simulation via Monte Carlo Algorithms on GPUs. *IEEE Latin Am. Trans.* **2014**, *12*, 491–498. https://doi.org/10.1109/TLA.2014.6827878.
45. Matadamas-Hernández, J.; Román-Alonso, G.; Rojas-González, F.; Castro-García, M. A.; Boukerche, A.; Aguilar-Cornejo, M.; Cordero Sánchez, S. Parallel Simulation of Pore Networks Using Multicore CPUs. *IEEE Trans. Comput.* **2014**, *63*, 1513–1525. DOI: https://doi.org/10.1109/TC.2012.197.
46. Halsey, G. Physical Adsorption on Non-Uniform Surfaces. *The Journal of Chemical Physics* **1948**, *16*, 931–937. DOI: https://doi.org/10.1063/1.1746689.
47. Casanova, F.; Chiang, C. E.; Li, C.-P.; Schuller, I. K. Direct Observation of Cooperative Effects in Capillary Condensation: The Hysteretic Origin. *Applied Physics Letters* **2007**, *91*, 243103. https://doi.org/10.1063/1.2822815.
48. 48. Sing, K. S. W. Reporting Physisorption Data for Gas/Solid Systems with Special Reference to the Determination of Surface Area and Porosity (Recommendations 1984). *Pure and Applied Chemistry* **1985**, *57*, 603–619. DOI: https://doi.org/10.1351/pac198557040603.
49. Gregg, S. J.; Sing, K. S. W.; Salzberg, H. W. Adsorption Surface Area and Porosity. *J. Electrochem. Soc.* **1967**, *114*, 279C. DOI: https://doi.org/10.1149/1.2426447.
50. Morishige, K. Hysteresis Critical Point of Nitrogen in Porous Glass: Occurrence of Sample Spanning Transition in Capillary Condensation. *Langmuir* **2009**, *25*, 6221–6226. DOI: https://doi.org/10.1021/la900022s.
51. Libby, B.; Monson, P. A. Adsorption/Desorption Hysteresis in Inkbottle Pores: A Density Functional Theory and Monte Carlo Simulation Study. *Langmuir* **2004**, *20*, 4289–4294. DOI: https://doi.org/10.1021/la036100a.
52. Ravikovitch, P. I.; Neimark, A. V. Density Functional Theory of Adsorption in Spherical Cavities and Pore Size Characterization of Templated Nanoporous Silicas with Cubic and Three-Dimensional Hexagonal Structures. *Langmuir* **2002**, *18*, 1550–1560. DOI: https://doi.org/10.1021/la0107594.
53. Rojas, F.; Kornhauser, I.; Felipe, C.; Esparza, J. M.; Cordero, S.; Domínguez, A.; Riccardo, J. L. Capillary Condensation in Heterogeneous Mesoporous Networks Consisting of Variable Connectivity and Pore-Size Correlation. *Phys. Chem. Chem. Phys.* **2002**, *4*, 2346–2355. https://doi.org/10.1039/b108785a.
54. Stauffer, D.; Aharony, A. Introduction To Percolation Theory, 0 ed.; Taylor & Francis, **2018**. https://doi.org/10.1201/9781315274386.
55. 55. Hidalgo-Olguín, D. R.; Cruz-Vázquez, R. O.; Alas-Guardado, S. J.; Domínguez-Ortiz, A. Lacunarity of Classical Site Percolation Spanning Clusters Built on Correlated Square Lattices. *Transp Porous Med* **2015**, *107*, 717–729. DOI: https://doi.org/10.1007/s11242-015-0463-3.
56. Everett, D. H. A General Approach to Hysteresis. Part 3.—A Formal Treatment of the Independent Domain Model of Hysteresis. *Trans. Faraday Soc.* **1954**, *50*, 1077–1096. DOI: https://doi.org/10.1039/tf9545001077.
57. Esparza, J. M.; Ojeda, M. L.; Campero, A.; Domínguez, A.; Kornhauser, I.; Rojas, F.; Vidales, A. M.; López, R. H.; Zgrablich, G. N2 Sorption Scanning Behavior of SBA-15 Porous Substrates.